Supplementary Materials for

AKR1B10 reprograms neutrophils by histone lactylation to foster immune evasion in KRAS^{G12C} mutation colorectal cancer liver metastasis

Weiwei Li[1†], Wenkang Yuan[1†], Zihao Du[1†], Xiangyu Wang[3†], Daoyue Wang[5,6], Songlin Xing[1], Tingting Shen[7], Canliang Lu[1], Jiale Chen[1], Anhai Yu[1], Xinyu Jiang[1], Shiwei Zhang[1], Shuhao Zheng[1], Xiaowen Feng[2,4], Tianqi Wang[1], Jieliang Zuo[8], Jinhong Chen[3*], Chao Zhang[1*], Xuefu Wang[2,4*] and Chong Zhang[1*]

[†]Weiwei Li, Wenkang Yuan, Zihao Du and Xiangyu Wang have contributed equally to this work.

[*]**Corresponding Authors**

Chong Zhang, Email: zhangchong@fy.ahmu.edu.cn. **Xuefu Wang**, Email: wangxuefu@ahmu.edu.cn. **Chao Zhang**, Email: chaozhang@fy.ahmu.edu.cn. **Jinhong Chen**, Email: jinhongch@hotmail.com.

This file includes:

Material and Methods

RNA sequencing (RNA-seq)

Tumor and cell samples used for RNA-seq were rapidly frozen in liquid nitrogen immediately after harvest. RNA-sequencing and data analysis services were provided by Shanghai Applied Protein Technology Co. Ltd. Gene ontology enrichment analysis was implemented by the DEGseq R package. Gene ontology terms with corrected cutoff value of log2 (fold change) > 1 and $p < 0.05$ were deemed to be significantly enriched by differentially expressed genes.

Collecting and processing of the multi-omics sequencing data

The single cell sequencing data of CRLM was collected from the sequencing database (HRR066493 and HRR066502). The bulk RNA-seq dataset (GSE159216) was got through the GEO database (https://www.ncbi.nlm.nih.gov/geo/). Further details regarding the methods used are provided in the supplementary information.

Cell proliferation assay

We used Cell Counting Kit-8 (CCK-8, Beyotime, C0038) to measure cell viability. Briefly, cells were inoculated into 96-well plates at a density of 3,000 cells per well, with 5 replicates in each group. Subsequently, the original culture medium was discarded at 24 h, 48 h and 72 h, and then 90 μL of empty medium mixed with 10 μL CCK-8 was newly added to each well. After the cells were incubated at 37 ℃ for 1 h, the absorbance was measured using an enzyme marker instrument at 450 nm.

Cell migration and invasion assay

For cell migration assay, the wound-healing assay was employed for evaluation. Cells were inoculated in six-well culture plates. When the cell confluence reaches 90%, a 200-μL pipette tip was used to make wounds. The cells were gently washed with PBS to eliminate any dislodged cells and cellular debris. After incubation with serum-free RPMI 1640 medium for 0 and 48 h, the distance of cell migration was recorded using a phase contrast microscopy. Cell invasion assay was assessed using matrigel-coated transwell membranes (8.0 μm pores, Corning). The upper chamber membrane was initially coated and incubated with a 1:8 mixture of matrigel and RPMI 1640 medium for 4 h. Subsequently, the upper chamber was inoculated with 50,000 cells in 200 μL of serum-free RPMI 1640 medium, while 600 μL of medium supplemented with 10% FBS was added to the lower chamber. Following 48 h of incubation, the migrated cells were fixed under 4% formaldehyde for 30 min and subsequently stained with

0.1% crystal violet for 15 min. Then, images were taken with an inverted microscope and the number of infiltrating cells was counted using ImageJ software. Quantitative analysis entailed the acquisition of images from five randomly chosen regions. Each experimental trial was replicated at least three times.

Conditioned medium (CM) preparation

Upon the cells attaining 90% confluence, substitute the original medium with fresh serum-free RPMI 1640 medium and continue to culture the cells for 24 h. Subsequently, the culture medium was collected and centrifuged at 2000 × g for 5 min to remove dead cells. The supernatant was filtered through a 0.22 μm filter and stored at -80 ℃ for further research.

Isolation of neutrophils and $CD8^+$ T cells

Mouse neutrophils were isolated from the bone marrow of 8 weeks BALB/c mice. In simple terms, the skin, muscle and fat on the femur and tibia of mice were removed completely. Then, the bone marrow cavity was rinsed with 27 G needle and RPMI 1640 medium to obtain the bone marrow single cell suspension. For human studies, the isolation of human neutrophils was derived from fresh peripheral blood of healthy blood donors. Subsequently, according to the manufacturer's instructions, neutrophils were isolated by density gradient centrifugation using the Mouse Bone Marrow Neutrophil Isolation Solution Kit (Solarbio, P8550) or Human Peripheral Blood Neutrophil Isolation Solution Kit (Solarbio, P9040) . For $CD8^+$ T cells, the MojoSort™ Human CD8 T Cell Isolation Kit (BioLegend, 480129) was used to isolation $CD8^+$ T cells in human fresh peripheral blood according to the manufacturer's instructions.

Neutrophil chemotaxis assay

Neutrophil chemotaxis assay was assessed using transwell membranes with 3.0 μm pores. A total of 1×10^6 freshly isolated neutrophils in 100 μL serum-free RPMI 1640 medium were added to the upper chambers, while CM from different tumor cells was added to the lower chambers. Following a 3 h incubation period, the cells that had traversed the membrane were fixed using 4% formaldehyde and subsequently stained with 0.1% crystal violet. The specific steps were the same as those of the cell invasion assay.

Determination of lactate concentration

Lactate concentration was measured using a Lactate Content Assay Kit (Solarbio, BC2230). Briefly, the tumor tissues and the collected CM were added with lactate extract and lactate assay buffer according to the corresponding steps to prepare the samples for the colorimetric lactate assay. The absorbance was immediately measured at 570 nm by spectrophotometric determination after sample preparation. Background absorbance was

subtracted during the statistical process.

Single-Cell RNA Sequencing Data Acquisition and Processing

All data analysis was performed in R (version4.5.0). Raw reads were imported into the Seurat pipeline (version5.3.0) using the Matrix package (version1.6.5). Low-quality cells were filtered via the dplyr package (version1.1.4). Doublets were removed using scDblFinder (version1.22.0). Quality control metrics were visualized with ggplot2 (version3.4.4), and plots were integrated using patchwork (version1.3.2). The filtered count matrix was normalized usingScaleData. Top 2000 highly variable genes were identified via FindVariableFeatures and used for Principal Component Analysis (PCA). Non-linear dimensionality reduction (UMAP/t-SNE) was conducted and the UMAP/t-SNE plots with cluster annotations were generated in ggplot2. Post-clustering statistics (cell count/proportion per cluster) were computed.

Bulk RNA-seq Processing

The methodology for analyzing immune infiltration from bulk RNA-seq data relies on computational deconvolution. This approach estimates the relative proportions of various immune cell types in a heterogeneous tissue sample based on its bulk gene expression profile.

Neutrophil Subclustering and Phenotypic Characterization

Neutrophil subpopulations were identified through unsupervised clustering and genes signature scoring. Single-cell RNA sequencing data were processed using Seurat. Neutrophils were extracted from the complete dataset based on canonical marker expression and subjected to further subclustering analysis.

Four distinct gene signatures were calculated using the AddModuleScore function in Seurat:

Glycolysis/lactate production signature: *HK2, HK3, GAPDH, PFKP, ALDOA, PGK1, LDHA, LDHB, PKM, ENO1;*

Lactate transport signature: *MCT1 (SLC16A1), MCT4 (SLC16A3), MCT2 (SLC16A7);*

Immunosuppressive signature: *CD274 (PD-L1), PDCD1LG2 (PD-L2), ARG1, IL10, TGFB1;*

Inflammatory signature: *IL1B, IL6, TNF, CXCL8, S100A8, S100A9.*

Neutrophils were subsequently re-clustered using the FindNeighbors and FindClusters functions (resolution = 0.5) based on the top 2000 variable genes identified by FindVariableFeatures. Dimensionality reduction was performed using RunPCA and RunUMAP (dims = 1:10). Neutrophil subtypes were classified based on median expression thresholds of the signature scores.

Interaction analysis between tumor cells and neutrophils

Cell-cell communication analysis was performed to investigate ligand-receptor interactions between tumor cells (malignant and proliferative epithelial cells) and neutrophil subpopulations using CellChat (v2.1.2). The CellChat object was created using subsetted data containing tumor cells and neutrophils, with cell identities defined by previously annotated clusters. Key ligand-receptor pairs were specifically analyzed, which included: *CXCL8-CXCR2, CXCL8-ACKR1, CSF3-CSF3R, CCL2-CCR2, CCL3-CCR1, CCL4-CCR5, VEGFA-FLT1, VEGFA-KDR, SPP1-CD44, SPP1-ITGAV_ITGB5* and *MIF-CD74_CXCR4*.

Communication probability was computed using computeCommunProb with default parameters, followed by pathway-level analysis and network aggregation (aggregateNet). For *CXCL8*-specific analysis, receptor expression patterns in neutrophil subtypes were examined for:

Primary CXCL8 receptors: *CXCR1, CXCR2, ACKR1, DPP4;*

Other chemokine receptors: *CCR1, CCR2, CCR5, CX3CR1, CXCR4;*

Pattern recognition receptors: *TLR2, TLR4, TLR8, NOD2, CLEC4E;*

Cytokine receptors: *IL1R1, IL1R2, IL6R, TNFRSF1A, TGFBR1.*

Interaction strength was calculated as the product of *CXCL8* expression in tumor cells and receptor expression in neutrophil subtypes, normalized to generate composite interaction scores. Visualization included network diagrams and bar plots highlighting the strongest *CXCL8*-receptor interactions across neutrophil subtypes.

Metabolic characterization of neutrophil subpopulations

Comprehensive metabolic profiling was performed by calculating signature scores for four key metabolic processes using the Seurat AddModuleScore function:

Lactate uptake: *SLC16A1 (MCT1), SLC16A3 (MCT4), SLC16A7 (MCT2), SLC16A8;*

Glycolytic capacity: *HK2, PFKP, PKM, GAPDH, LDHA, ALDOA, PGK1, PGAM1, ENO1;*

Energy metabolism: *ATP5A1, ATP5B, COX5A, CYCS, NDUFA1, SDHA, UQCRC1.*

PD-1/PD-L1 axis analysis between $CD8^+$ T Cells and neutrophils

The immunosuppressive potential of neutrophil subpopulations was evaluated through PD-1/PD-L1 axis

analysis with $CD8^+$ cytotoxic T lymphocytes. $CD8^+$ T cells were identified as "$CD8^+$ Cytotoxic T Lymphocytes" (cluster 14) based on expression of *CD8A, CD8B, GZMB, PRF1* and so on.

PD-L1 (CD274) expression patterns across neutrophil subpopulations were analyzed. Interaction potential was assessed by creating a PD-1/PD-L1 interaction matrix, with interaction strength calculated as the product of PD-1 expression in $CD8^+$ T cells and PD-L1 expression in neutrophil subpopulations. Network visualization highlighted the PD-1/PD-L1 interactions between $CD8^+$ T cells and neutrophil subpopulations, with edge weights proportional to interaction strength.

A

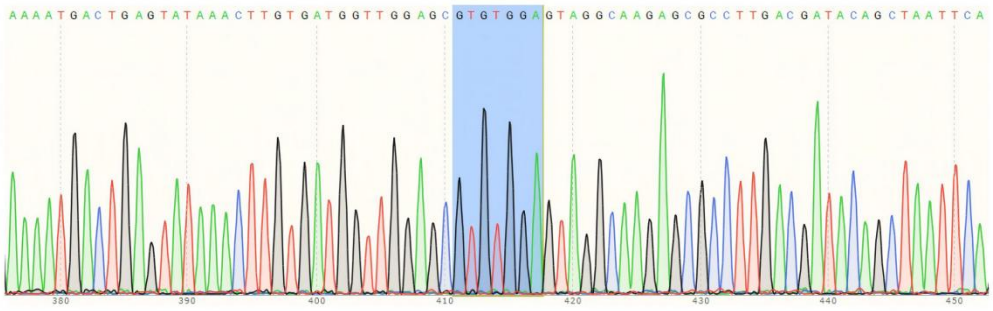

B

DNA sequencing information

	Met	Thr	Glu	Tyr	Lys	Leu	Val	Met	Val	Gly	Ala	Cys	Gly	Val	Gly	Lys	Ser	Ala	Leu	Thr	Ile	Gln
GAAAATGACT			GAGTATAAAC			TTGTGATGGT				TGGAGCGTGT			GGAGTAGGCA			AGAGCGCCTT			GACGATACAG		
CTTTTACTGA			CTCATATTTG			AACACTACCA				ACCTCGCACA			CCTCATCCGT			TCTCGCGGAA			CTGCTATGTC		

Figure S1. The sequencing verification successfully obtained the homozygous CT26 cells with KRAS p.G12C mutation.

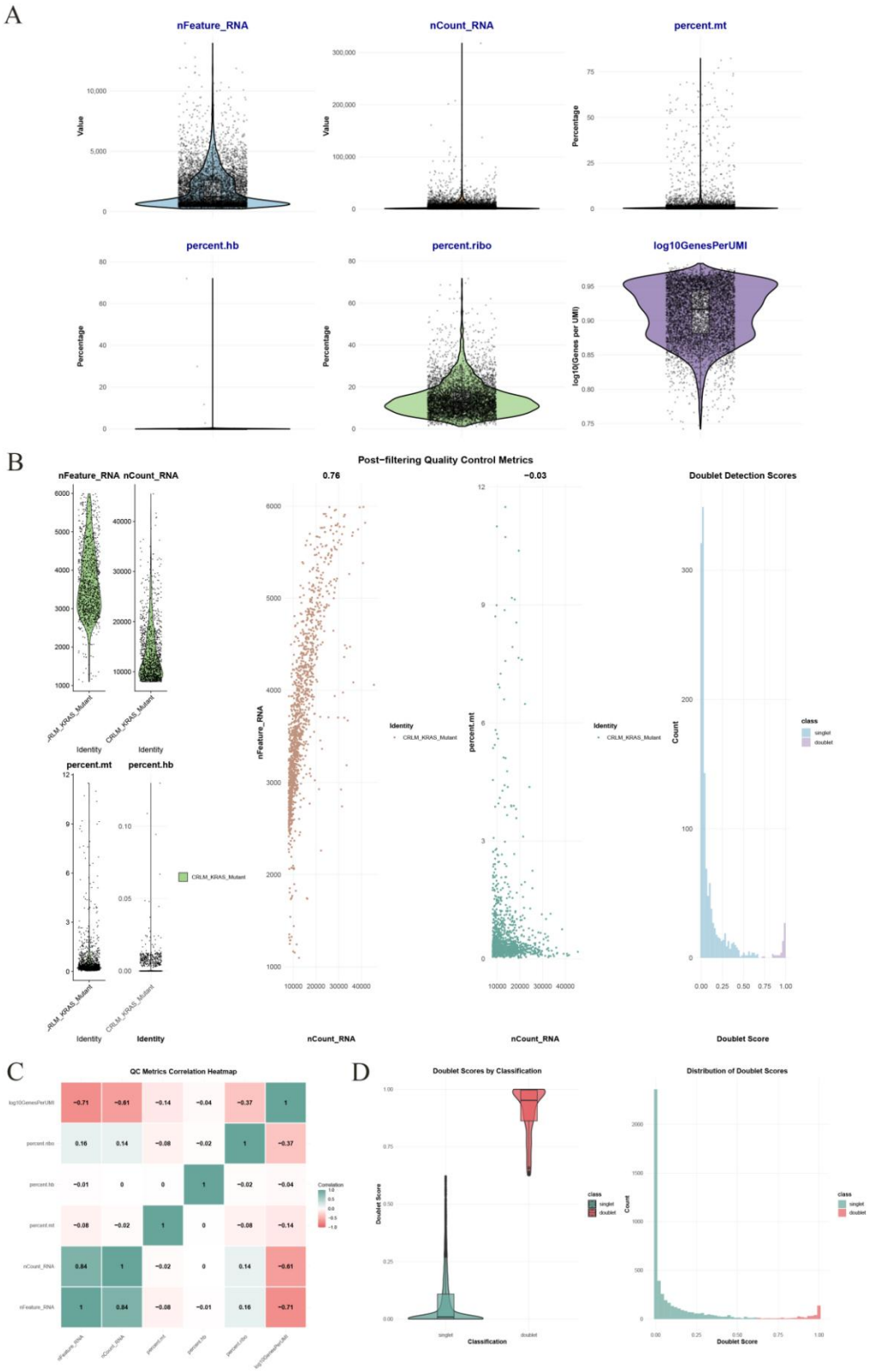

Figure S2. Single-cell data quality control and cell filtration for KRAS mutation CRLM.

(A) Pre-filtering quality control metrics. **(B)** Post-filtering quality control metrics. **(C)** Quality control metrics correlation heatmap. **(D)** Apply the scDblFinder to define and identify the dual states of cells and filter out the

unqualified detection parts.

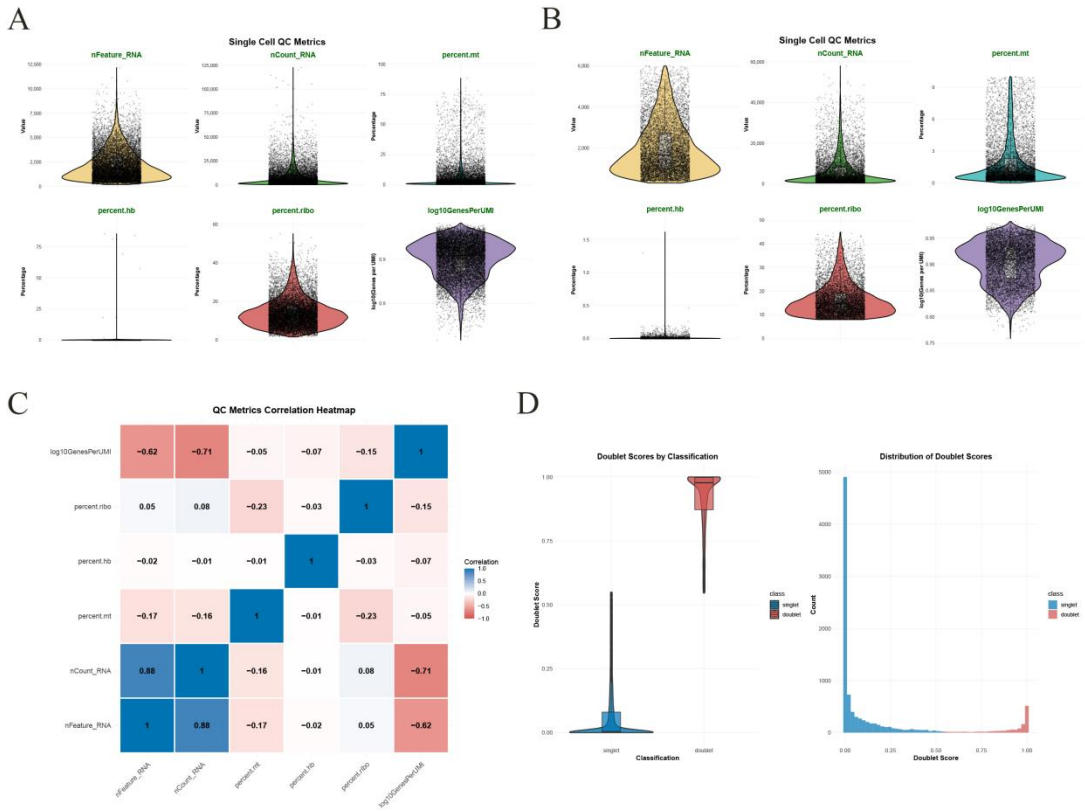

Figure S3. Single-cell data quality control and cell filtration for wild-type CRLM.

(A) Pre-filtering quality control metrics. **(B)** Post-filtering quality control metrics. **(C)** Quality control metrics correlation heatmap. **(D)** Apply the scDblFinder to define and identify the dual states of cells and filter out the unqualified detection parts.

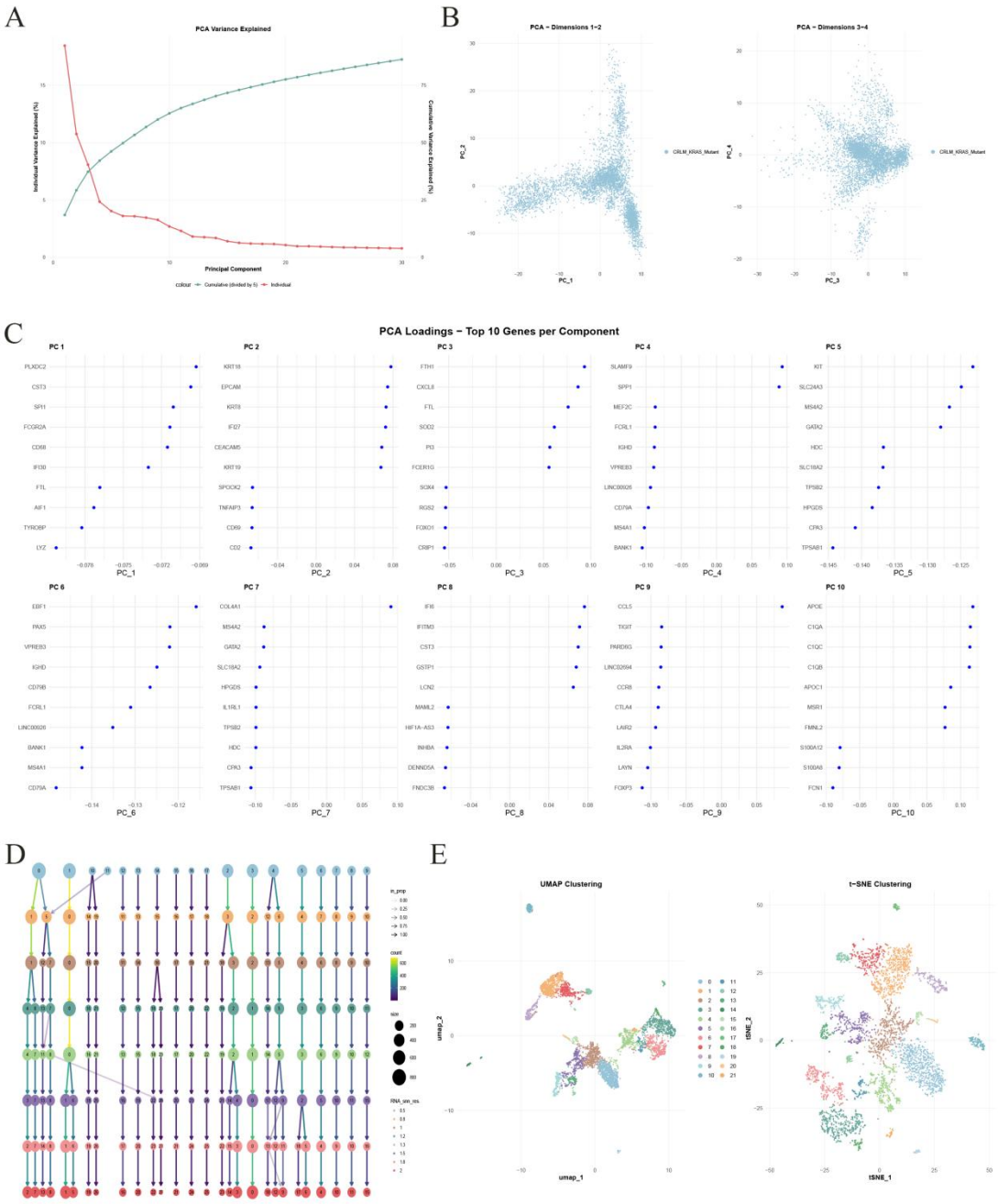

Figure S4. Cell clustering results based on KRAS mutation CRLM single-cell data.

(A-C) The results of determining the optimal clustering parameters by applying the principal component analysis (PCA) algorithm. **(D)** Dynamic clustering tree represented the process of clustering of cell clusters as the resolution changes. **(E)** UMAP and TSNE illustrated the comparison of the distribution of different cell clusters.

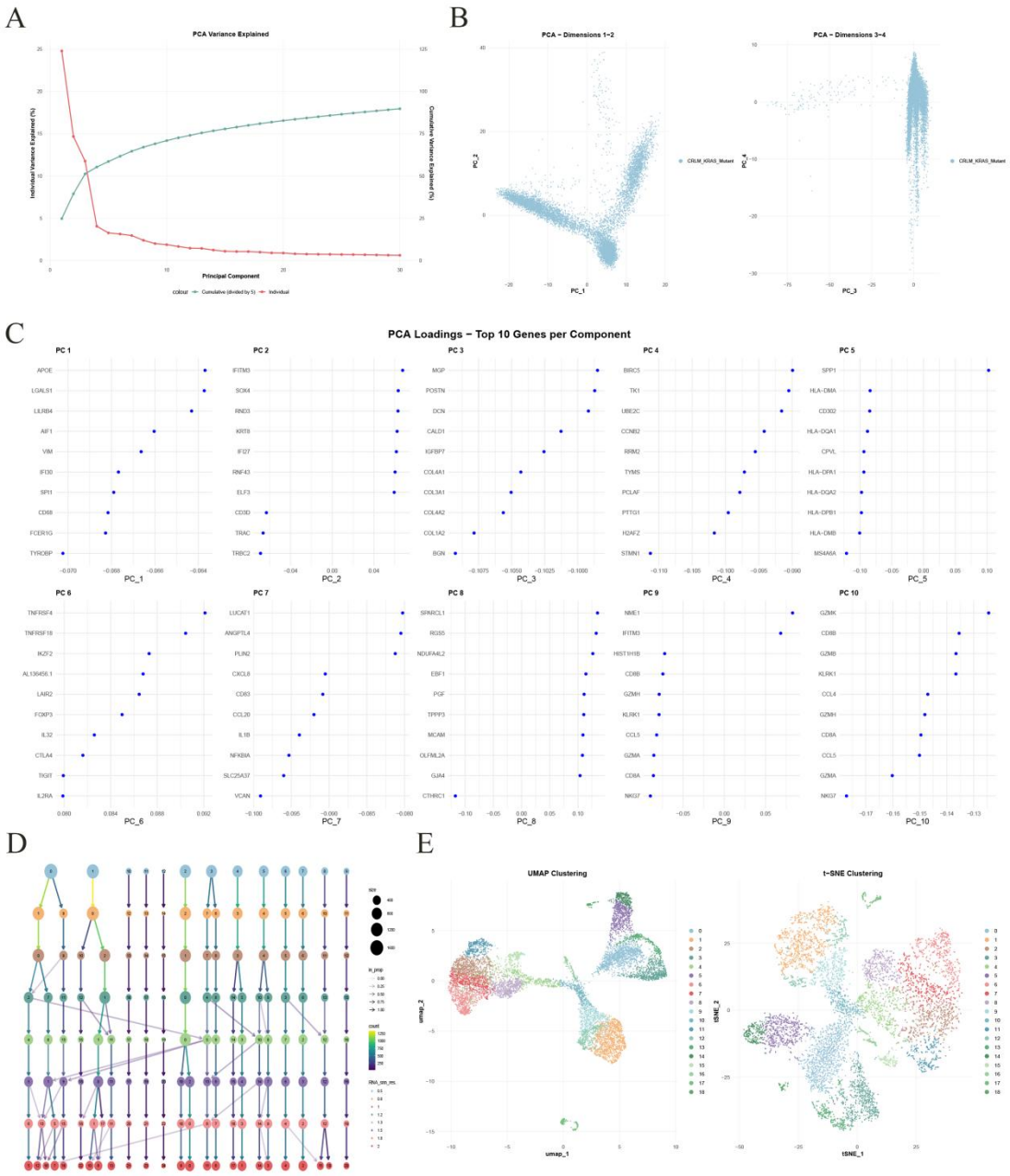

Figure S5. Cell clustering results based on wild-type CRLM single-cell data.

(A-C) The results of determining the optimal clustering parameters by applying the principal component analysis (PCA) algorithm. **(D)** Dynamic clustering tree represented the process of clustering of cell clusters as the resolution changes. **(E)** UMAP and TSNE illustrated the comparison of the distribution of different cell clusters.

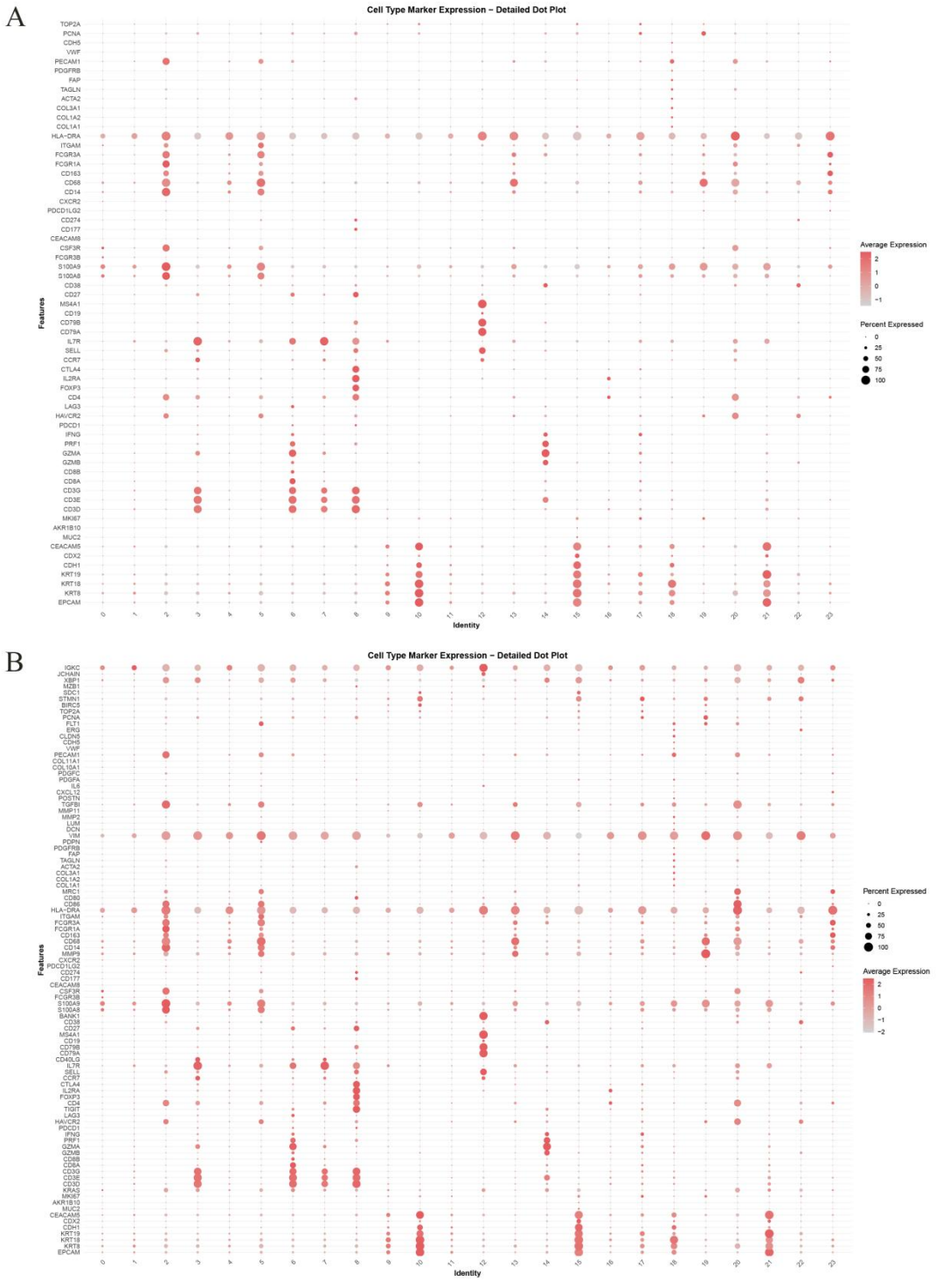

Figure S6. Annotation of diffenrent cell subtypes from KRAS mutation CRLM predicted by the SingleR algorithm (A) and marker genes (B).

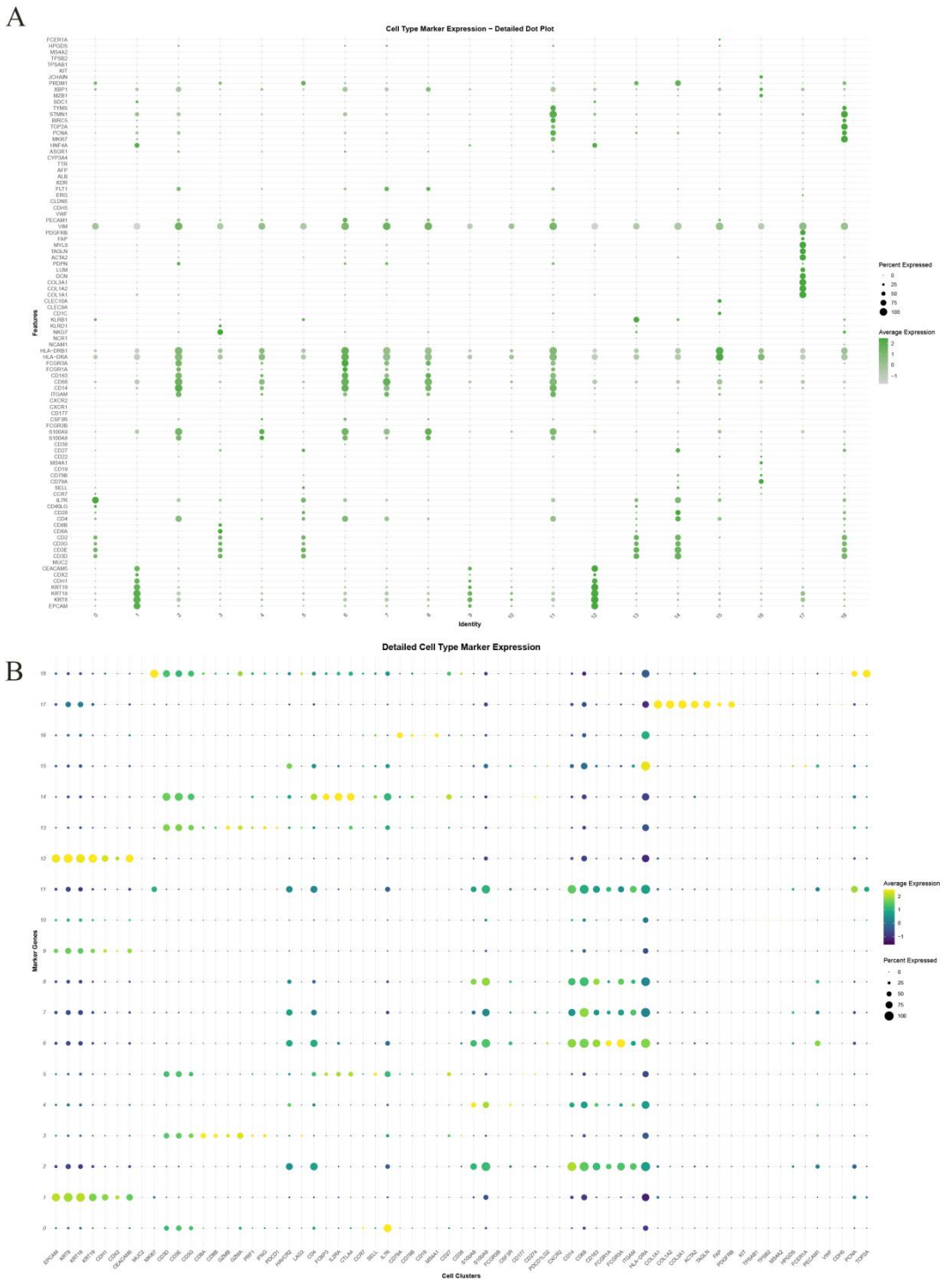

Figure S7. Annotation of diffenrent cell subtypes from wild-type CRLM predicted by the SingleR algorithm (A) and marker genes (B).

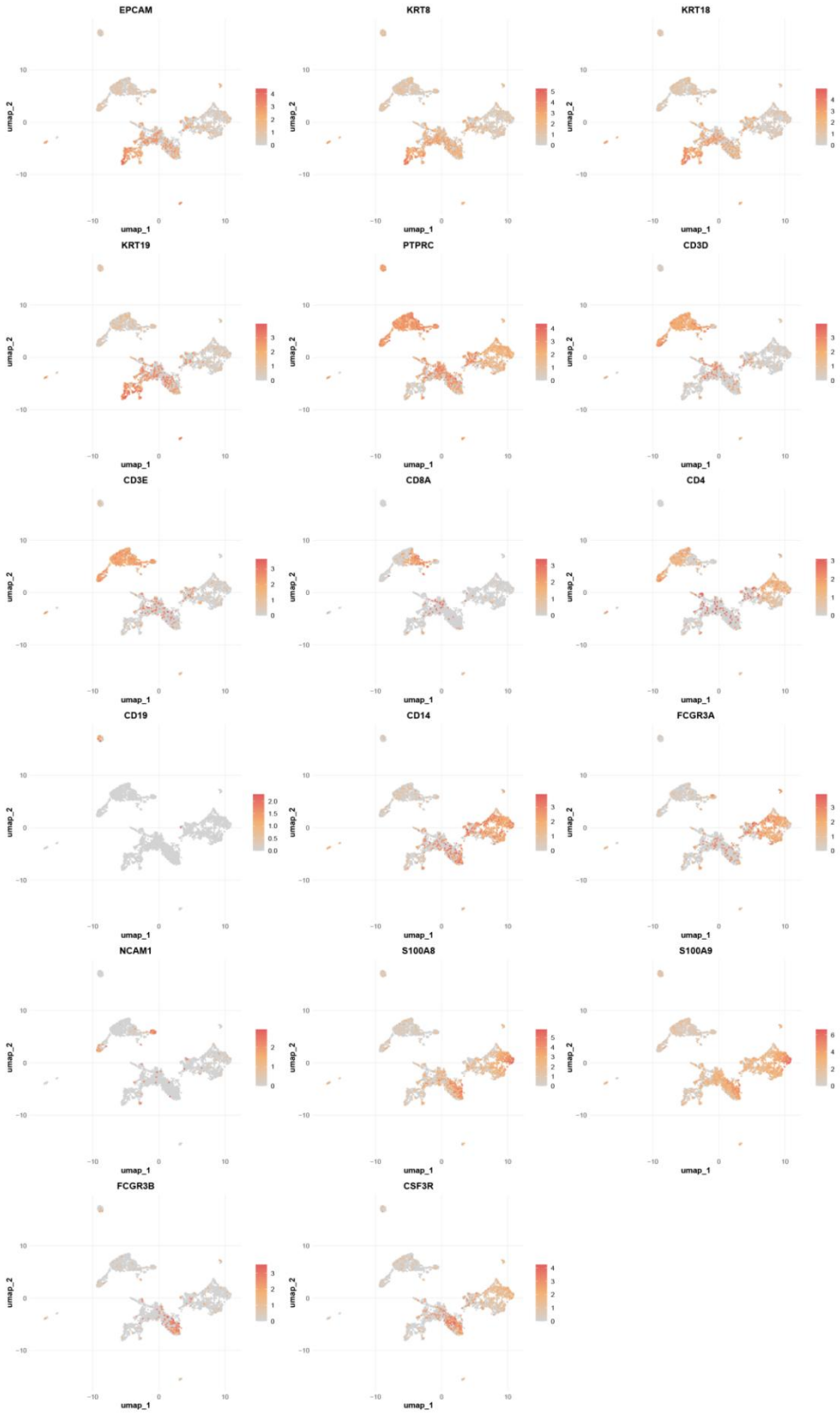

Figure S8. Umap showed the expression and distribution of marker genes in each single cell cluster from the KRAS mutation CRLM sample.

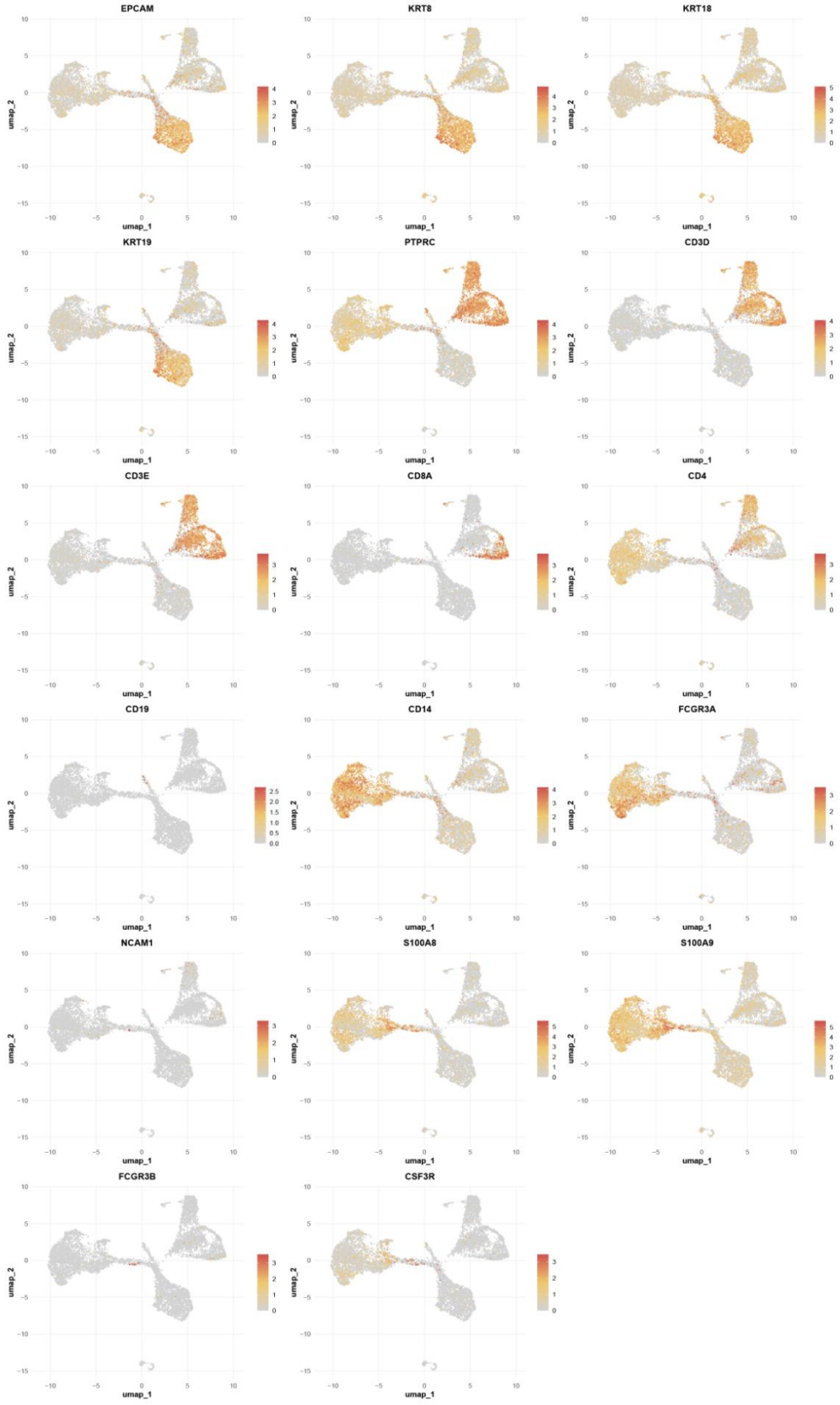

Figure S9. Umap showed the expression and distribution of marker genes in each single cell cluster from the wild-type CRLM sample.

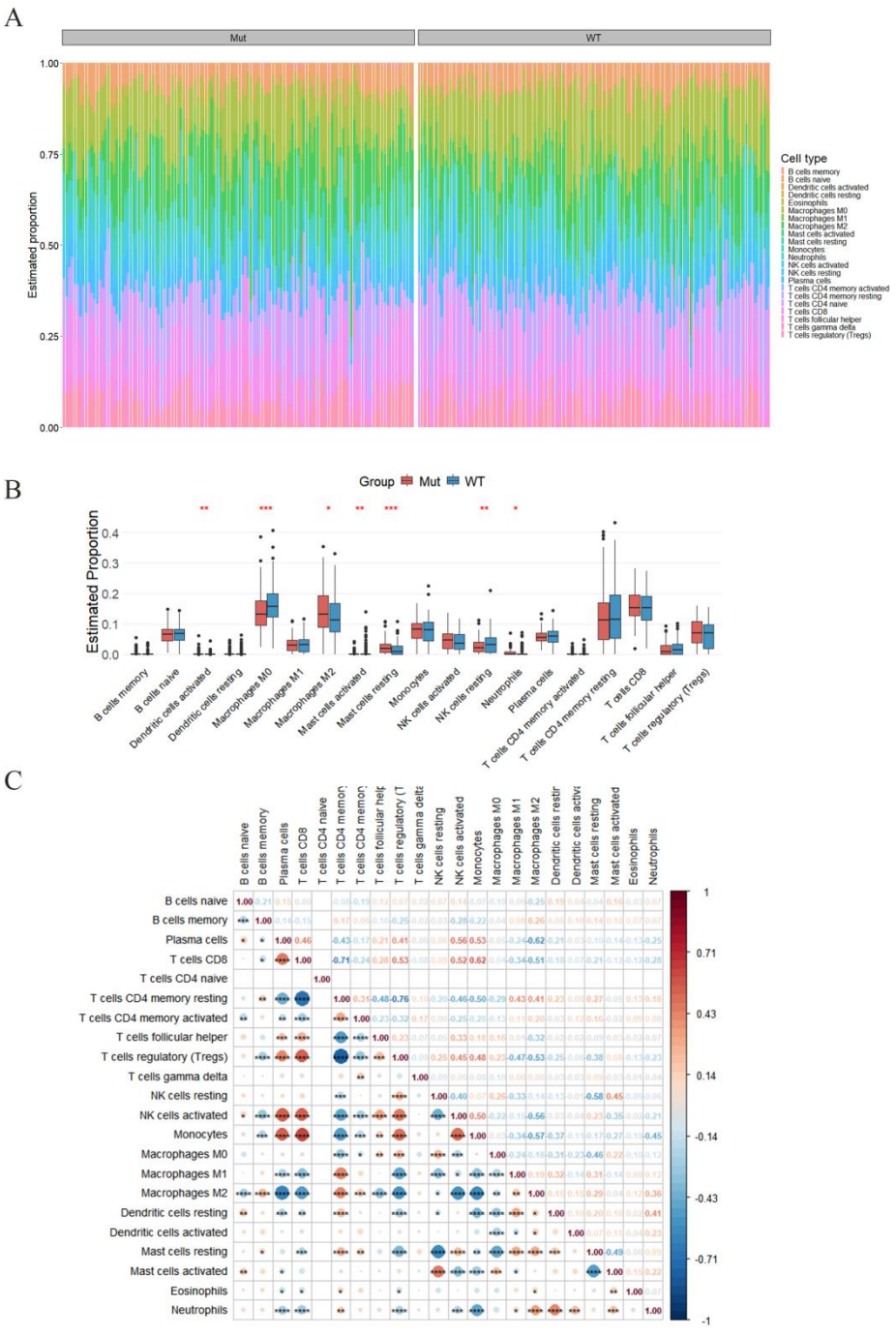

Figure S10. Comparative analysis of differences in immune infiltration from bulk RNA-seq data.

(A) The corresponding proportion of the degree of immune cell infiltration within each individual. **(B)** Comparison of immune infiltration differences between the KRAS mutation group and the wild-type group samples based on Bulk RNA Seq. **(C)** Pearson correlation analysis among immune cell infiltration scores within the KRAS mutation group samples.

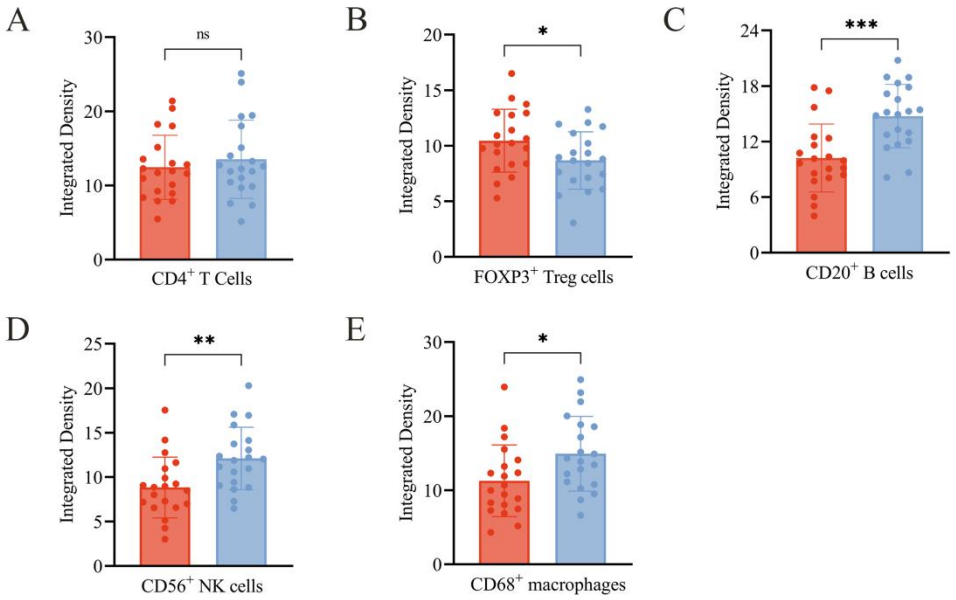

Figure S11. Quantification of major immune cells density in KRAS^{G12C} mutation and wild-type CRLM cases.

(A-E) Immune cells mainly include CD4$^+$ T cells (A), FOXP3$^+$ Treg cells (B), CD20$^+$ B cells (C), CD56$^+$ NK cells (D) and CD68$^+$ macrophages (E).

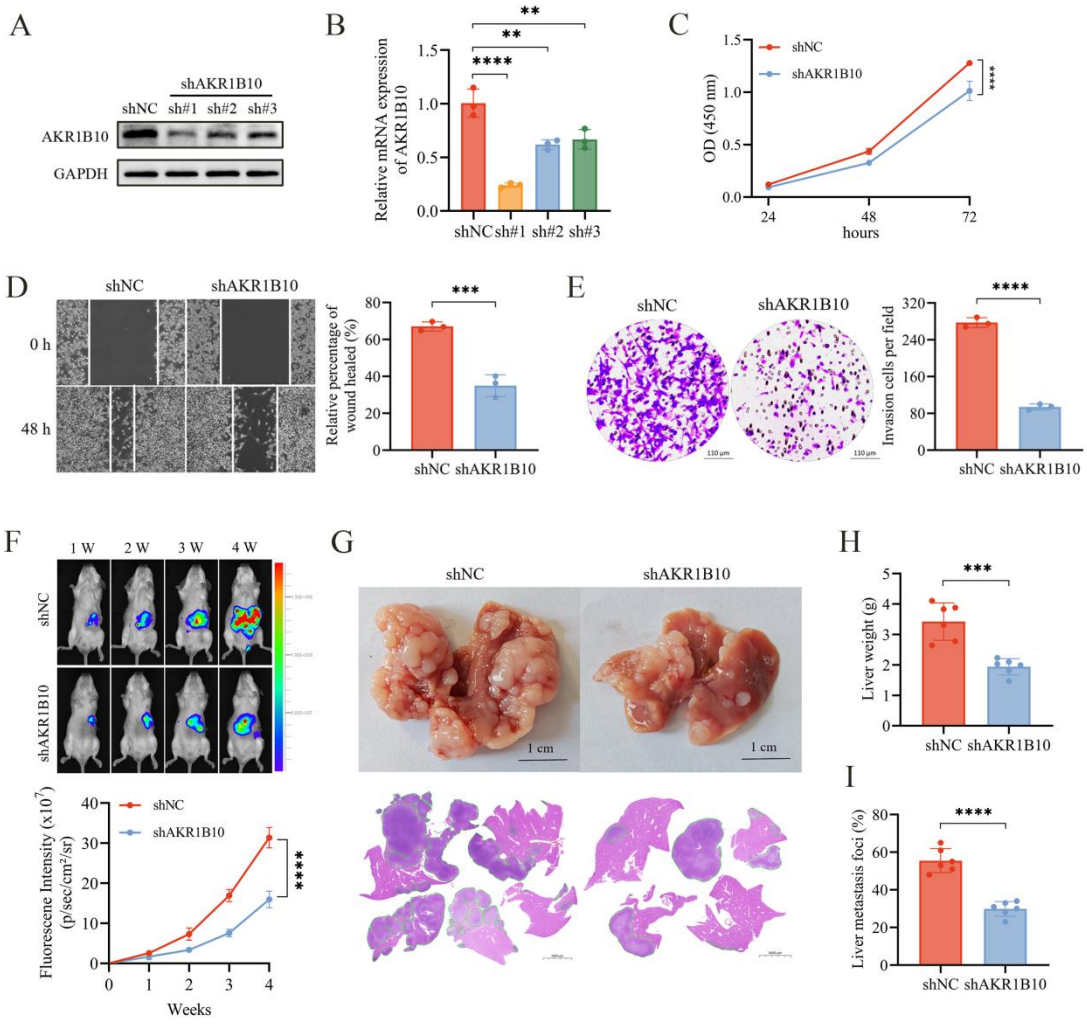

Figure S12. The knockdown of AKR1B10 alleviated the progression of the KRAS^{G12C} mutation CRLM.

(A, B) The knockdown efficiency of AKR1B10 in CT26K cells was verified at protein and mRNA levels. **(C)** Cell viability was monitored by CCK-8 assay. **(D)** Representative images and the rate of wound closure from the wound healing assay with shNC and shAKR1B10 cells. **(E)** Representative images and number of cells from transwell assays with shNC and shAKR1B10 cells. **(F, G)** Representative fluorescence images (F), gross images and HE images (G) of liver metastasis in the shNC and shAKR1B10 groups of CRLM models. **(H, I)** Liver weight (H) and percentage of liver metastasis foci in the liver (I) of shNC and shAKR1B10 groups mice.

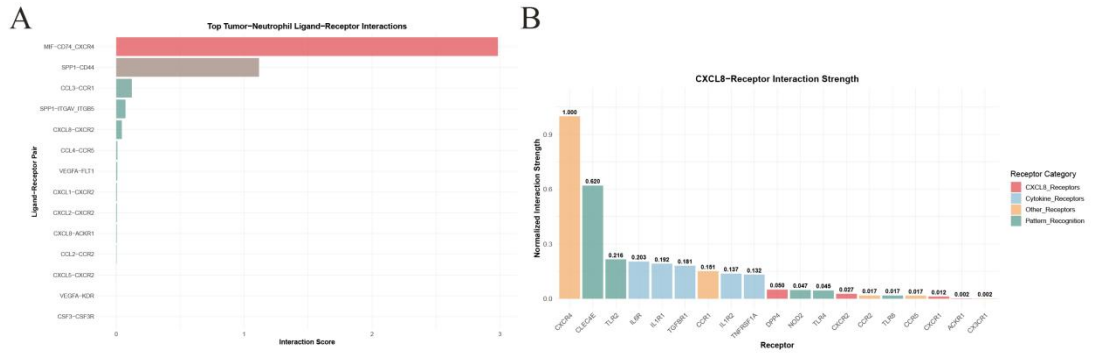

Figure S13. The strength of interaction between tumor cells and neutrophils.

(A) Ranking of the interaction intensity of the classical communication axis between tumor cells and neutrophils.

(B) The differences in the interaction strength between multiple types of receptors on neutrophils and CXCL8 expressed in tumor cells.

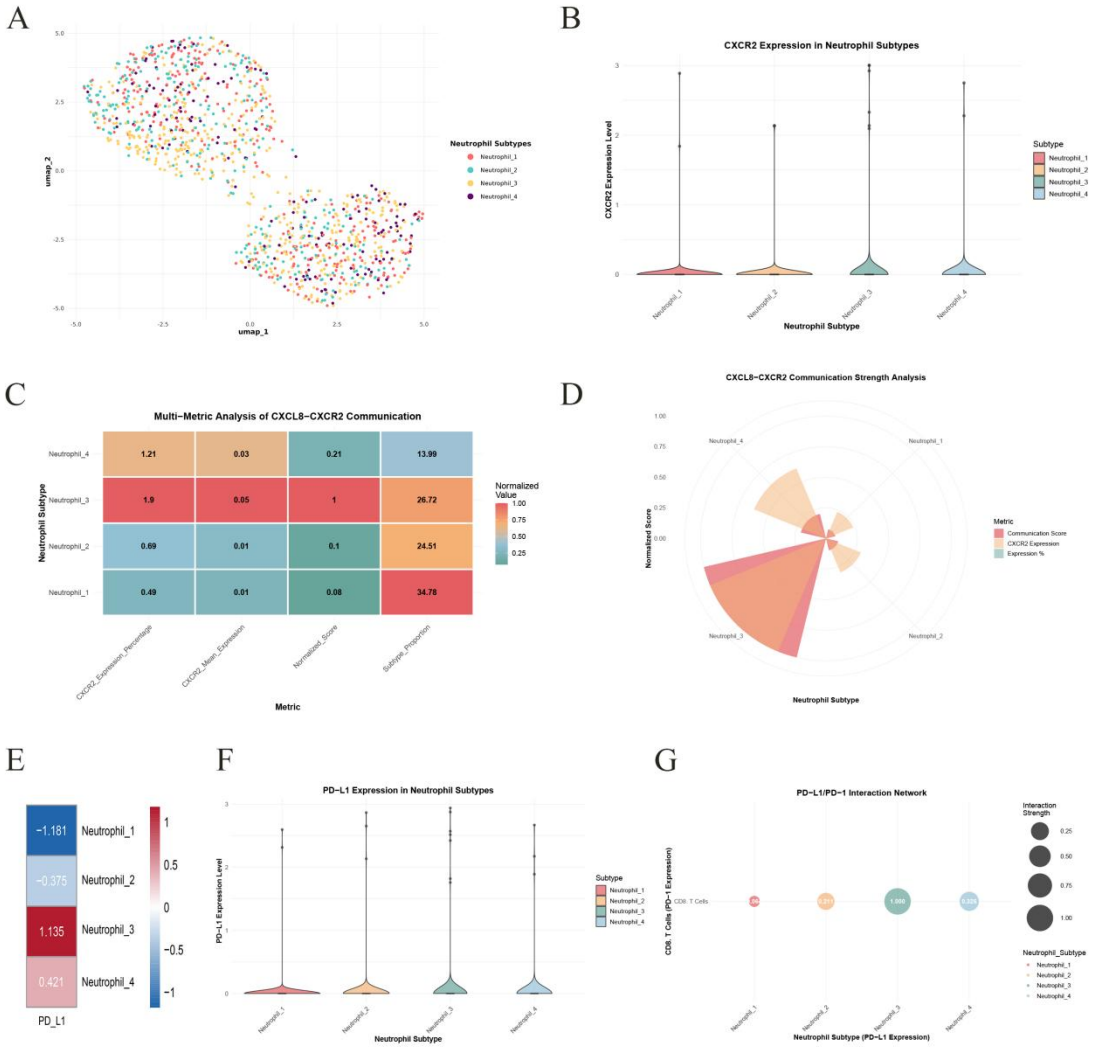

Figure S14. Heterogeneity of neutrophils in KRAS mutation CRLM.

(A) The UMAP showed the spatial distribution of neutrophil subpopulations (neutrophil_1-4). Each dot represents a single cell. Color represents corresponding cell cluster as indicated. **(B)** Differential expression of CXCR2 in different neutrophil subpopulations. **(C)** Heat map of metabolic characteristics multi-metric analysis of CXCL8/CXCR2 communication corresponding to neutrophil subpopulations. **(D)** The radar chart of the differences in the interaction intensity of the CXCL8/CXCR2 axis among the four neutrophil subpopulations. **(E, F)** The expression differences of PD-L1 in different neutrophil subpopulations. **(G)** The differences in the interaction strength between four neutrophil subpopulations and $CD8^+$ T cells through PD-1/PD-L1 axis.

Table S1. Clinicopathological characteristics of CRLM patients underwent liver resction.

Clinicopathological characteristics	FAH Cohort (n=59)	HSH Cohort (n=370)	P value
Gender (%)			
Male	39 (66.1)	241 (65.1)	0.885
Female	20 (33.9)	129 (34.9)	
Age (%)			
≤ 55 years	19 (32.2%)	116 (31.4%)	0.896
> 55 years	40 (67.8%)	254 (68.6%)	
Time to metastasis (%)			
Metachronous	23 (39.0)	118 (31.9)	0.282
Synchronous	36 (61.0)	252 (68.1)	
Primary tumor location (%)			
left	41 (69.5)	290 (78.4)	0.248
right	15 (25.4)	71 (19.2)	
Both sides	3 (5.1)	9 (2.4)	
pT stage (%)			
Tis-T2	13 (22.0)	58 (15.7)	0.222
T3-T4	46 (78.0)	312 (84.3)	
pN stage (%)			
N0	23 (39.0)	135 (36.5)	0.712
N1-N2	36 (61.0)	235 (63.5)	
AJCC stage (%)			
I-II	11 (18.6)	53 (14.3)	0.387
III-IV	48 (81.4)	317 (85.7)	
Tumor grade (%)			
G1-G2	45 (76.3)	271 (73.2)	0.624
G3	14 (23.7)	99 (26.8)	

Number of liver metastases (%)			
Single	33 (55.9)	138 (37.3)	0.007
Multiple	26 (44.1)	232 (62.7)	
Distribution of liver metastases (%)			
Unilobar	45 (76.3)	207 (55.9)	**0.003***
Bilobar	14 (23.7)	163 (44.1)	
Size of liver metastases (%)			
< 5cm	51 (86.4)	301 (81.4)	0.344
≥ 5cm	8 (13.6)	69 (18.6)	
Neoadjuvant chemotherapy (%)			
Yes	32 (54.2)	153 (41.4)	0.063
No	27 (45.8)	217 (58.6)	
Gene status (%)			
$KRAS^{G12C}$ mutation	26 (44.1)	126 (34.1)	0.135
Wild-type	33 (55.9)	244 (65.9)	

*P value <0.05 is marked in bold.

FAH, the First Affiliated Hospital of Anhui Medical University; HSH, Huashan Hospital Fudan University; CRLM, colorectal cancer liver metastases.

Table S2. Primer sequences and shRNAs uesd in this study.

Primers for RT-qPCR		
Gene	Forward primer (5'-3')	Reverse primer (5'-3')
H-β-actin	CCCTGGAGAAGAGCTACGAG	GGAAGGAAGGCTGGAAGAGT
H-AKR1B10	TCAGAATGAACATGAAGTGGGG	TGGGCCACAACTTGCTGAC
M-AKR1B10	CTAGTGCCAAACCAGAGGACC	TCCTGTATTCGAGAAGGTGTCA
M-β-actin	GGCTGTATTCCCCTCCATCG	CCAGTTGGTAACAATGCCATGT
M-CXCL1	ACTGCACCCAAACCGAAGTC	TGGGGACACCTTTTAGCATCTT
M-CXCL2	CCAACCACCAGGCTACAGG	GCGTCACACTCAAGCTCTG
M-CXCL5	GTTCCATCTCGCCATTCATGC	GCGGCTATGACTGAGGAAGG
M-CXCL6	GTTCCATCTCGCCATTCATGC	GCGGCTATGACTGAGGAAGG
M-CXCL8	TCGAGACCATTTACTGCAACAG	CATTGCCGGTGGAAATTCCTT
M-TGFβ	CCACCTGCAAGACCATCGAC	CTGGCGAGCCTTAGTTTGGAC
M-LDHA	CAAAGACTACTGTGTAACTGCGA	TGGACTGTACTTGACAATGTTGG
M-GLUT1	GCAGTTCGGCTATAACACTGG	GCGGTGGTTCCATGTTTGATTG
M-HK2	ATGATCGCCTGCTTATTCACG	CGCCTAGAAATCTCCAGAAGGG
M-PKM2	CGCCTGGACATTGACTCTG	GAAATTCAGCCGAGCCACATT
Primers for shRNA		
shNC	TTCTCCGAACGTGTCACGT	
shAKR1B10#1	GGGCATCACCATCACAGCCTA	
shAKR1B10#2	ACCAGAGGACCCCCTATTACT	
shAKR1B10#3	GCACAAGAGGACTGCAGCACA	
Primers for Chip		
Gene	Forward primer (5'-3')	Reverse primer (5'-3')
PD-L1	GCTCCAAAGGACTTGTACGTG	TGATCTGAAGGGCAGCATTTC

Table S3. Information of the antibodies used in this study.

Antibody	Company	Cat No.	Usage
AKR1B10	Fine Test	FNab10610	WB, IHC
GAPDH	Proteintech	60004-1-Ig	WB
CD3	Bioss	bs-10498R	IF
CD4	Abcam	ab133616	IF
CD8	Abcam	ab178089	IF
CD66b	Abcam	Ab300122	IF
CD68	Abcam	ab213363	IF
PD-1	CST	86163S	IF
PD-L1	CST	13684S	IF
FoxP3	Abcam	ab20034	IF
CD20	Dako	IR604	IF
CD56	Abcam	ab75813	IF
Pan-Lactyl-Lysine	PTM Bio	PTM-1401RM	WB, IF
Lactyl-Histone H3 (Lys9)	PTM Bio	PTM-1419RM	WB, IF, Chip
Lactyl-Histone H3 (Lys14)	PTM Bio	PTM-1414RM	WB
Lactyl-Histone H3 (Lys18)	PTM Bio	PTM-1427RM	WB, IF, Chip
Lactyl-Histone H3 (Lys23)	PTM Bio	PTM-1413RM	WB
Lactyl-Histone H3 (Lys27)	PTM Bio	PTM-1428	WB
Lactyl-Histone H4 (Lys8)	PTM Bio	PTM-1415RM	WB
Lactyl-Histone H4 (Lys12)	PTM Bio	PTM-1411RM	WB
Lactyl-Histone H4 (Lys16)	PTM Bio	PTM-1417RM	WB
Histone H3	PTM Bio	PTM-1001RM	WB
Histone H4	PTM Bio	PTM-1015RM	WB

Table S4. Fluorescent-labeled antibodies used in this study.

Marker	Fluorescence	Item	Brand
LIVE/DEAD	BV510	423102	BioLegend
CD45	FITC	103108	BioLegend
CD3	APC/Fire™ 750	100248	BioLegend
CD4	Brilliant Violet 605™	100548	BioLegend
CD8	PE/Cyanine 7	100722	BioLegend
CD11b	APC	101212	BioLegend
Ly6G	PE/Cyanine 7	127618	BioLegend
CD69	PE	104508	BioLegend
PD-1	Brilliant Violet 421™	135218	BioLegend
PD-L1	PE	124307	BioLegend
TIM-3	APC	119706	BioLegend
TNFα	PE	506306	BioLegend
IFNγ	APC	505810	BioLegend

Table S5. Correlation between clinicopathological features and AKR1B10 expression of CRLM patients.

	$KRAS^{G12C}$ mutation			Wild-type		
Clinicopathological characteristics	High AKR1B10 (n = 76)	Low AKR1B10 (n = 76)	P value	High AKR1B10 (n = 138)	Low AKR1B10 (n = 139)	P value
Gender (%)						
Male	40 (52.6)	48 (63.2)	0.189	90 (65.2)	48 (73.4)	0.141
Female	36 (47.4)	28 (36.8)		48 (34.8)	28 (26.6)	
Age (%)						
≤ 55 years	25 (32.9)	22 (28.9)	0.599	52 (37.7)	36 (25.9)	0.035
> 55 years	51 (67.1)	54 (71.1)		86 (62.3)	103 (74.1)	
Time to metastasis (%)						
Metachronous	28 (36.8)	25 (32.9)	0.610	36 (26.1)	52 (37.4)	**0.043***
Synchronous	48 (63.2)	51 (67.1)		102 (73.9)	87 (62.6)	
Primary tumor location (%)						
left	46 (60.5)	52 (68.4)	0.084	115 (83.3)	118 (84.9)	0.916
right	30 (39.5)	21 (27.6)		18 (13.0)	17 (12.2)	
Both sides	0 (0.0)	3 (4.0)		5 (3.7)	4 (2.9)	
pT stage (%)						
Tis-T2	9 (11.8)	16 (21.1)	0.126	21 (15.2)	31 (22.3)	0.131
T3-T4	67(88.2)	62 (81.6)		117 (84.8)	108 (77.7)	
pN stage (%)						
N0	15 (19.7)	34 (44.7)	**<0.001***	46 (33.3)	63 (45.3)	**0.041***
N1-N2	61 (80.3)	42 (55.3)		92 (66.7)	76 (54.7)	
Tumor grade (%)						

G1-G2	48 (63.2)	63 (82.9)	**0.006***	94 (68.1)	111 (79.9)	**0.026***
G3	28 (36.8)	13 (17.1)		44 (31.9)	28 (20.1)	
Number of liver metastases (%)						
Single	25 (32.9)	45 (59.2)	**0.001***	45 (34.2)	56 (40.3)	0.184
Multiple	45 (59.2)	31 (40.8)		93 (65.8)	83 (59.7)	
Distribution of liver metastases (%)						
Unilobar	42 (55.3)	51 (67.1)	0.134	75 (54.3)	84 (60.4)	0.306
Bilobar	34 (44.7)	25 (32.9)		63 (45.7)	55 (39.6)	
Size of liver metastases (%)						
< 5 cm	62 (81.6)	63 (82.9)	0.832	116 (84.1)	111 (79.9)	0.363
≥ 5 cm	14 (18.4)	13 (17.1)		22 (15.9)	28 (20.1)	
Neoadjuvant chemotherapy (%)						
Yes	44 (57.9)	28 (36.8)	**0.009***	53 (38.4)	60 (43.2)	0.420
No	32 (42.1)	48 (63.2)		85 (61.6)	79 (56.8)	

*P value <0.05 is marked in bold.

CRLM, colorectal cancer liver metastases.